

Mitigation of Converter-Grid Resonance, Grid-Induced Distortion, and Parametric Instabilities in Converter-Based Distributed Generation

Yasser Abdel-Rady Ibrahim Mohamed, *Member, IEEE*

Abstract—This paper presents a robust interfacing scheme for distributed generation (DG) inverters featuring robust mitigation of converter-grid resonance at parameter variation, grid-induced distortion, and current-control parametric instabilities. The proposed scheme relies on a high-bandwidth current-control loop, which is designed with continuous wideband active damping against converter-grid disturbances and parametric uncertainties by providing adaptive internal-model dynamics. First, a predictive current controller with time-delay compensation is adopted to control the grid-side current with high-bandwidth characteristics to facilitate higher bandwidth disturbance rejection and active-damping control at higher frequencies. Second, to ensure high disturbance rejection of grid distortion, converter resonance at parameter variation, and parametric instabilities, an adaptive internal model for the capacitor voltage and grid-side current dynamics is included within the current-feedback structure. Due to the time-varying and periodic nature of the internal-model dynamics, a neural-network-based estimator is proposed to construct the internal-model dynamics in real time. Theoretical analysis and comparative experimental results are presented to demonstrate the effectiveness of the proposed control scheme.

Index Terms—Digital control, distributed generation (DG), grid-converter resonance, pulsewidth-modulated (PWM) inverters.

I. INTRODUCTION

THE ENVIRONMENTAL regulations due to greenhouse gas emission, the electricity business restructuring, and the recent development in small-scale power generation are the main factors driving the energy sector into a new era, where large portions of increases in electrical energy demand will be met through widespread installation of distributed resources or what is known as distributed generation (DG) [1]. The majority of distributed resources are interfaced to the utility grid via dc–ac inverter systems [2]. However, the dynamic and uncertain nature of a distribution network challenges the control and stability of the DG interface system. The fact that a typical distribution system is faced with unavoidable disturbances and uncertainties

complicates the design of a practical plug and play inverter-based DG interface.

In the grid-connected mode, various grid disturbances can be imposed on the DG interface. Important among these are the interaction between the converter, grid impedance, and grid distortion. Difficulties occur in the following ways.

- 1) Depending on the grid configuration, a large set of grid impedance values is yielded, as DG is commonly installed in weak grids with long radial distribution feeders [3], [4]. Furthermore, in the context of smart-grid solutions, grid reconfiguration for self-healing and grid-performance optimization remarkably affects the grid parameters at the point of common coupling (PCC). Therefore, plug-and-play integration of DG units under different grid conditions is a key requirement in the smart-grid environment. In addition, cable overload, saturation and temperature effects are all reasons for possible variation in the interfacing impedance seen by the inverter. The interfacing impedance variations directly affect the stability of the local system at the PCC. Further, it can remarkably shift the resonance frequency of the converter. In this case, the injected current will be highly distorted and it can propagate through the system and drive other voltage and current harmonics.
- 2) There is a strong trend toward the use of current control for pulsewidth-modulated (PWM) voltage-sourced inverters (VSIs) in DG systems [2], [5], [6], which offers the possibility of high power-quality injection when it is properly designed. In this approach, it is commonly desired to design the inner current-control loop with high-bandwidth characteristics to ensure accurate current tracking, to shorten the transient period as much as possible and to force the VSI to equivalently act as a current-source amplifier with high disturbance rejection against grid distortion [7]. However, the sensitivity of the dominant poles of the closed-loop current controller becomes very high to uncertainties in total interfacing impedance (the impedance seen by the inverter at the PCC, which is a function of the grid impedance), particularly with high feedback gains (e.g., deadbeat response). The instability of the current-control loop accompanied by the saturation effect of the pulsewidth modulator leads to sustained oscillations in the injected current.
- 3) The voltage at the PCC directly affects the control performance of the DG inverter. Due to the proliferation of nonlinear loads, the grid voltage at the PCC is more likely to be distorted [8], [9], particularly in weak grids

Manuscript received January 12, 2010; revised April 11, 2010 and June 28, 2010; accepted August 8, 2010. Date of current version June 10, 2011. Recommended for publication by Associate Editor F. Wang.

The author is with the Department of Electrical and Computer Engineering, University of Alberta, Edmonton, AB T6G 2V4, Canada (e-mail: yasser_rady@ieee.org).

Color versions of one or more of the figures in this paper are available online at <http://ieeexplore.ieee.org>.

Digital Object Identifier 10.1109/TPEL.2010.2070878

with long radial distribution feeders. The grid-voltage distortion and unbalance drive harmonic currents and increase the distortion in the exported power. Furthermore, large-scale integration of power-electronic-interfaced distributed resources remarkably increases the bandwidth of grid distortion. High-frequency power-quality events can be a crucial factor that limits the penetration level of distributed resources [10].

Mitigation of such grid-converter interactions is one of the important functions that should be found in a current-controlled DG unit. From the point of view of robustness against grid harmonics and unbalance, the compensation capability of the low-order harmonics in the case of proportional–integral (PI) current controllers, either in the stationary or the synchronous reference frames, is very poor, yielding a major drawback when they are used in grid-connected and microgrid systems. Resonant controllers, tuned for selective harmonics elimination, can relax this problem. However, these controllers are tuned at preset frequencies and the stability is not verifiably guaranteed for a large band of harmonic cancellations. These drawbacks are obvious in [8], where a stationary-frame resonant controller for grid-side current regulation is proposed. The same drawbacks can be seen in [11], where resonant synchronous-frame controllers are emerged in the current-control structure to mitigate the effect of grid harmonics. An additional stability issue in existing controllers, either in the stationary or the synchronous reference-frame, is the interaction with variation in grid inductance and ac-side filter parameters. Instability is yielded when a mismatch in the grid inductance or ac-side filter parameters shifts the bandwidth of the current controller to be lower than any of the resonant frequencies.

Different active-damping solutions are proposed to damp the converter resonance phenomenon in grid-connected converters. In [4], a lead–lag compensator is proposed to damp the high-frequency converter resonance and current-controller low-frequency instability due to grid-impedance and filter parameter interactions. The compensator parameters, however, should be tuned at different values of the grid impedance. In [12], a filter-based active-damping technique is proposed. The active-damping performance is optimized for a given set of system conditions by using a genetic algorithm. In [13], a capacitor-split technique is adopted, where the current between the two capacitors is measured to simplify the power-circuit dynamics. Besides the filter compactness and packaging issues associated with this method, the stability is not verifiably guaranteed under parameter variation. In [8], a multiloop control algorithm is proposed, where an inner capacitor-current-control loop is adopted. However, additional sensors and control complexity are yielded. More importantly, the stability is not guaranteed at parameter variation and with wide range of background grid distortion. Analysis and comparison of different additional feedback active damping techniques are presented in [14].

Existing active-damping controllers, with the exception of [15], provide active-damping control performance at fixed and known resonance and/or critical frequencies, which is an optimistic assumption. In fact, practical implementation of an active-damping controller is challenging as the active-damping

poles should be located close to the system poles and zeros; this indicates that small uncertainty in system parameters leads to instability [16]. To overcome this problem, a robust linear matrix inequalities (LMI)-based controller is presented in [15] to yield a stable performance for a large set of grid conditions without using self-tuning algorithms. Improved robust control performance is obtained; however, the robustness range is limited and only the grid impedance is selected as an uncertain system parameter. Further, the nominal control performance cannot be guaranteed even within the predefined robustness range required by the LMI controller. The problem becomes more challenging when the ratio of the sampling and resonance frequencies is relatively low.

These facts challenge the stability and the control effectiveness of a current-controlled DG interface, particularly in weak and microgrids, where the grid stiffness is very low.

Motivated by the aforementioned limitations, this paper presents a robust DG interface featuring robust mitigation of converter-grid resonance at parameter variation, grid-induced distortion, and current-control parametric instabilities. The conceptual design of the proposed control scheme is to avoid gain shaping at harmonic frequencies and to provide continuous energy shaping using the estimated lump sum of internal-model dynamics. The proposed design does not require a self-tuning procedure; does not assume predefined set of system parameters; and inherently considers uncertainties in the filter and grid parameters in the presence of grid distortion. A high-bandwidth current-control loop is designed with continuous wideband active damping against converter-grid disturbances and parametric uncertainties. First, a predictive current controller with delay compensation is adopted to control the grid-side current. The delay compensation method forces the delays elements, which are caused by voltage calculation, pulsedwidth modulation (PWM), and synchronous-frame rotation to be equivalently placed outside the close-loop control system. Hence, their effect on the closed-loop stability is eliminated and the current controller can be designed with high-bandwidth characteristics to facilitate higher bandwidth of disturbance rejection and active-damping control at higher frequencies. Second, to ensure effective disturbance rejection of grid distortion, converter resonance at parameter variation, and parametric instabilities, an adaptive internal model for the capacitor voltage and grid-side current dynamics is included within the current-feedback structure. Due to the time-varying and periodic nature of the internal-model dynamics, a neural network (NN)-based estimator is proposed to construct the internal-model dynamics in real time. The adaptive ability of NNs in learning process dynamics facilitates feasible and easy adaptation design at different grid disturbances and operating conditions [17]–[19].

The remainder of this paper is structured as follows. In Section II, modeling and analysis of a three-phase current-controlled grid-connected VSI with *LCL* filter are presented. In Section III, the proposed control scheme is described. Evaluation results are provided to demonstrate the effectiveness of the proposed interfacing scheme in Section IV. Conclusions are drawn in Section V.

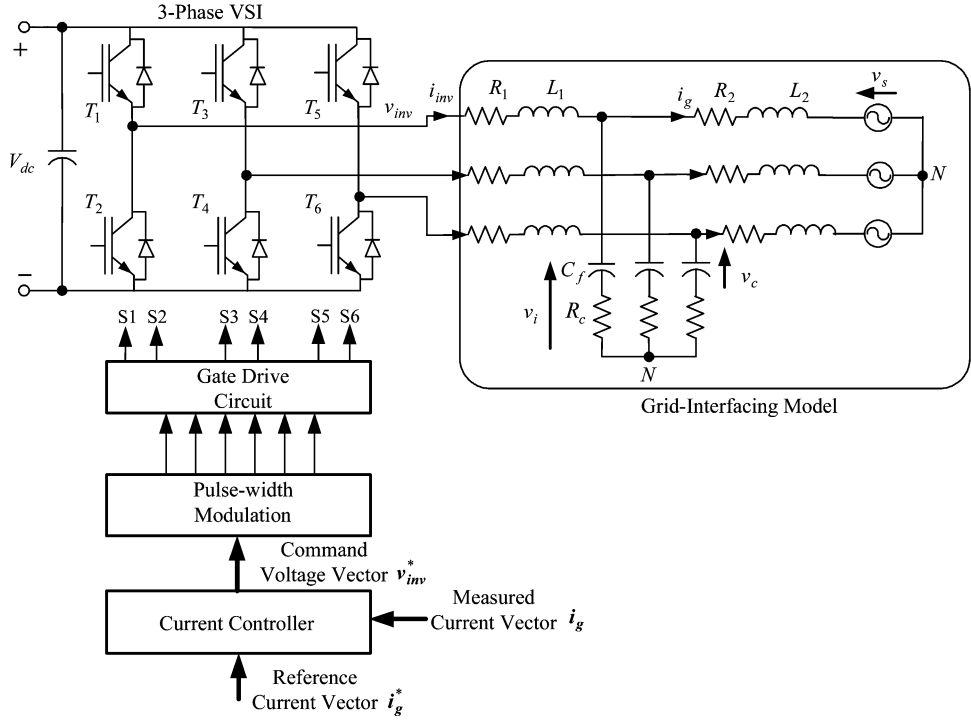


Fig. 1. Grid-connected three-phase VSI with an inner current-control loop and T -type LCL filter.

II. MODELING AND ANALYSIS OF THREE-PHASE CURRENT-CONTROLLED GRID-CONNECTED VSI WITH LCL FILTER

A system topology of a grid-connected current-controlled VSI with a T -type LCL filter is depicted in Fig. 1, where R_1 and L_1 represent the resistance and inductance of the inverter-side filter inductor; R_2 and L_2 represent the equivalent resistance and inductance of the grid-side filter inductor and the grid resistance and inductance at the PCC; C_f is the filter capacitance; R_c is the effective resistance in the capacitive branch; v_s is the grid voltage; v_c is the filter capacitor voltage; v_i is the intermediate voltage; i_g is the injected grid current; i_{inv} is the inverter output current; and v_{inv} is the inverter output voltage.

In the natural reference frame, the per-phase power-circuit dynamics can be represented by the following model:

$$L_1 \frac{di_{inv}}{dt} = v_{inv} - v_i - R_1 i_{inv} \quad (1)$$

$$L_2 \frac{di_g}{dt} = v_i - v_s - R_2 i_g \quad (2)$$

$$C_f \frac{dv_c}{dt} = i_{inv} - i_g. \quad (3)$$

The open-loop undamped dynamics of the power circuit can be represented in the complex frequency domain by (4), shown at the bottom of this page, where s is the Laplace operator.

Under conventional PI control, the closed-loop current-control dynamics can be given by (5), shown at the bottom of this page, where K_P and K_I are the proportional and integral

$$\begin{aligned} I_g(s) &= \frac{1}{L_1 L_2 C_f s^3 + C_f (L_1 R_2 + L_2 R_1) s^2 + (R_1 R_2 C_f + L_1 + L_2) s + (R_1 + R_2)} V_{inv}(s) \\ &\quad - \frac{(L_1 C_f s^2 + R_1 C_f s + 1)}{L_1 L_2 C_f s^3 + C_f (L_1 R_2 + L_2 R_1) s^2 + (R_1 R_2 C_f + L_1 + L_2) s + (R_1 + R_2)} V_s(s) \end{aligned} \quad (4)$$

$$\begin{aligned} I_g(s) &= \frac{K_p s + K_I}{L_1 L_2 C_f s^4 + C_f (L_1 R_2 + L_2 R_1) s^3 + (R_1 R_2 C_f + L_1 + L_2) s^2 + (R_1 + R_2 + K_p) s + K_I} I_g^*(s) \\ &\quad - \frac{L_1 C_f s^3 + R_1 C_f s^2 + s}{L_1 L_2 C_f s^4 + C_f (L_1 R_2 + L_2 R_1) s^3 + (R_1 R_2 C_f + L_1 + L_2) s^2 + (R_1 + R_2 + K_p) s + K_I} V_s(s) \end{aligned} \quad (5)$$

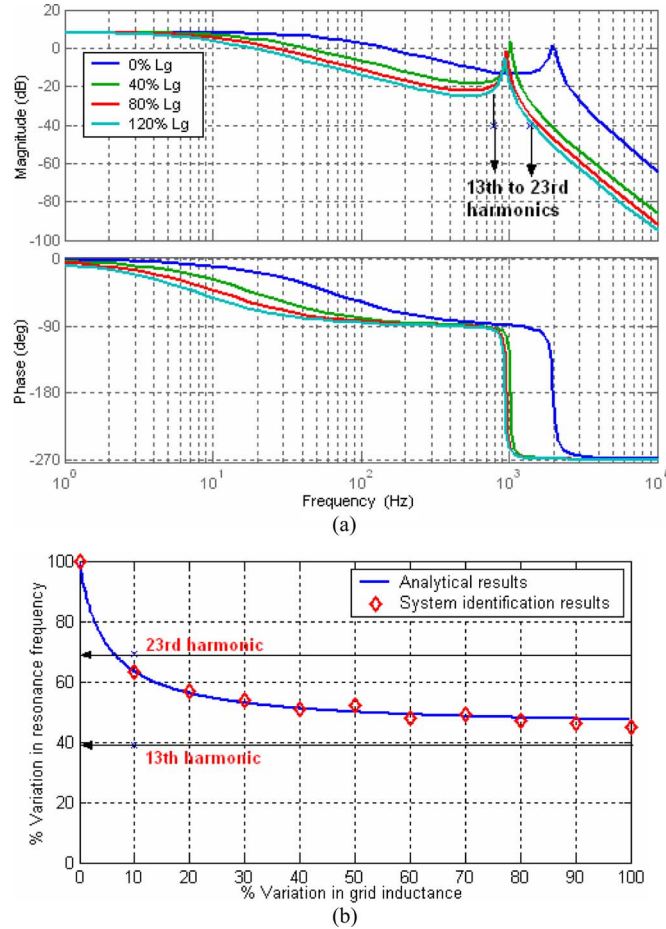


Fig. 2. Variation of the resonance frequency with the grid inductance (% of 5.8 mH). (a) Frequency characteristics of the harmonics impedance. (b) Variation of the resonance frequency with the percentage variation in interfacing inductance.

gains of the PI controller, and the superscript “*” denotes the reference value.

Using (5), the closed-loop harmonic impedance of the converter can be given by (6), as shown at the bottom of the next page.

Fig. 2 shows the frequency characteristics of a 200-kW converter with *LCL* filter, switching frequency 5 kHz, and nominal resonance frequency 2 kHz. The resonance frequency should be sufficiently lower than the switching frequency to utilize the third-order attenuation effect of the *LCL* filter. Fig. 2(a) indicates that the harmonic impedance at low-order harmonics is obviously weak. Fig. 2(a) and (b) shows the variation of the resonance frequency with the percentage variation in interfacing inductance, either in the filter inductor or the grid impedance. It can be seen that small drift in the interfacing inductance (e.g., 20% mismatch) can shift the resonance frequency to almost 60% of its nominal value. Accordingly, harmonic excitation may easily occur at low-order harmonics. Further, Fig. 2 indicates that the current-tracking, disturbance rejection, and active damping of the resonant dynamics cannot be handled by a simple single-degree-of-freedom (DOF) PI controller.

To enhance the disturbance rejection performance, proportional harmonic resonant controllers (P-HRESSs) can be applied

to provide internal-model dynamics at selected harmonic frequencies. The transfer function of the P-HRES is defined as

$$G_{\text{P-HRES}}(s) = k_p + \sum_{h=1}^n \frac{k_{ih}s}{s^2 + (h\omega_o)^2} \quad (7)$$

where k_p is the proportional gain, h is the harmonic order, k_{ih} is the resonant filter gain at harmonics h , n is the upper limit of harmonic order, and ω_o is the fundamental angular frequency. The proportional resonant controller can reduce the effect of the grid-induced harmonics in the injected currents; however, the stability is not verifiably guaranteed under interfacing parameter variation. Instability occurs once one or more of the resonant frequencies lie outside the loop bandwidth. Evaluation results in Fig. 9 illustrate these facts.

III. CONTROL-SYSTEM DEVELOPMENT

Fig. 3 shows the proposed control scheme for a current-controlled DG interface. The control scheme consists of a high-bandwidth current-control system, NN-based internal-model generator, and robust phase-locked loop (PLL). Theoretical analysis and design procedure of the proposed control scheme are described in the following sections.

A. Improved Power-Circuit Model

The power-circuit dynamics can be modeled as a decoupled linear disturbed system. This can be achieved by considering the grid-side current i_g and its derivative $d_i_g = \dot{i}_g$ as augmented biases imposed on the inverter-side output current. The direct result of this modeling approach is the inherent decoupling between the *LC* filter circuit and the grid-side inductor. Therefore, a robust control approach for controlling the grid-side current in a deadbeat manner can be realized.

In the natural reference frame, the per-phase power-circuit dynamics can be represented by the following model:

$$\frac{dx_1}{dt} = \mathbf{A}_{tc}x_1 + \mathbf{B}_{tc}v_{inv} \quad (8)$$

$$v_i = \mathbf{c}^T x_1 \quad (9)$$

$$\frac{di_g}{dt} = a_c i_g + b_c v_i + g_c v_s \quad (10)$$

where

$$\mathbf{x}_1 = \begin{bmatrix} i_{inv} \\ v_c \\ i_g \\ d_i_g \end{bmatrix} \quad \mathbf{A}_{tc} = \begin{bmatrix} -(R_1 + R_c) & -1 & R_c & 0 \\ \frac{1}{L_1} & \frac{-1}{L_1} & \frac{R_c}{L_1} & 0 \\ \frac{1}{C_f} & 0 & 0 & 0 \\ 0 & 0 & 0 & 1 \end{bmatrix}$$

$$\mathbf{B}_{tc} = \begin{bmatrix} \frac{1}{L_1} \\ 0 \\ 0 \\ 0 \end{bmatrix} \quad \mathbf{C} = [R_c \quad 1 \quad -R_c \quad 0]$$

$$a_c = \frac{-R_2}{L_2} \quad b_c = \frac{1}{L_2} \quad g_c = \frac{-1}{L_2}$$

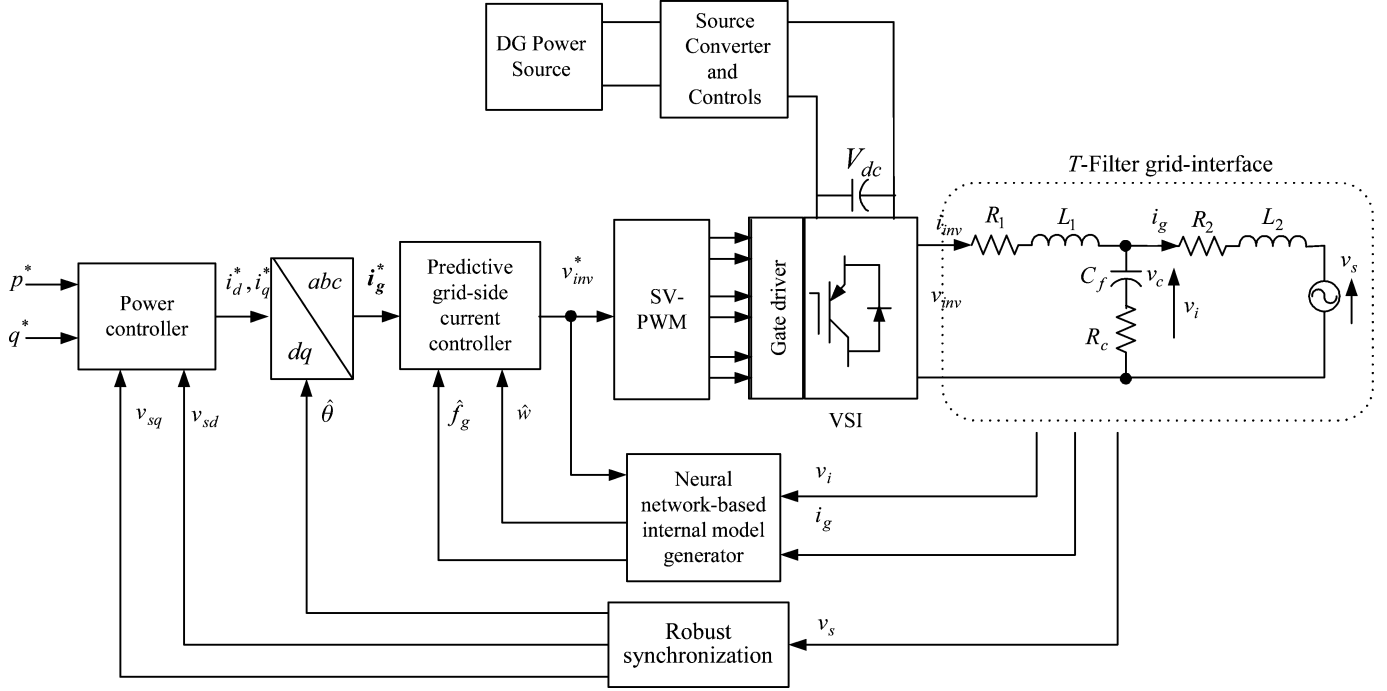


Fig. 3. Proposed control scheme.

The modeling approach in this paper is generalized by considering the effective resistance of the capacitive branch R_c . System identification results indicate that a nontrivial resistance exists in a practical LCL filter due to the frequency-dependent losses in the power circuit and the effective charging resistance [20]. However, the damping provided by this resistance is not enough to effectively damp the power-circuit resonance and interactions with grid inductance. On the other hand, ignoring this amount of inherent damping leads to overdesigned damping solutions.

Since the harmonic components included in the inverter output voltage are not correlated with the sampled reference currents and with a symmetric output voltage, the PWM VSI can be assumed as a zero-order hold circuit with a transfer function $H(s)$

$$H(s) = \frac{1 - e^{-sT}}{s} \quad (11)$$

where T is the discrete-time control sampling period.

For digital implementation of the control algorithm, the power-circuit dynamics in (8)–(10) can be represented in a discrete-time domain with the conversion $H(s)$ in (11), as follows:

$$x_1(k+1) = \mathbf{A}_{td}x_1(k) + \mathbf{B}_{td}v_{inv} \quad (12)$$

$$v_i(k) = \mathbf{c}^T \mathbf{x}_1(k) \quad (13)$$

$$i_g(k+1) = a_d i_g(k) + b_d v_i(k) + g_d v_s(k) \quad (14)$$

where \mathbf{A}_{td} , \mathbf{B}_{td} , a_d , b_d , and g_d are the sampled equivalents of the continuous-time system matrices and parameters. If the continuous system is sampled with interval T , which is at least ten times shorter than the power-circuit lowest time constant, then the discrete-time system parameters can be approximated as follows:

$$\mathbf{A}_{td} = e^{\mathbf{A}_{tc}T} \cong \begin{bmatrix} 1 - \frac{T(R_1 + R_c)}{L_1} & -\frac{T}{L_1} & \frac{TR_c}{L_1} & 0 \\ \frac{T}{C_f} & 1 & -\frac{T}{C_f} & 0 \\ 0 & 0 & 1 & T \\ 0 & 0 & 0 & 1 \end{bmatrix} \quad (15)$$

$$\mathbf{B}_{td} = \int_0^T e^{\mathbf{A}_{tc}\tau} d\tau \cdot \mathbf{B}_{tc} \cong \begin{bmatrix} \frac{T}{L_1} \\ 0 \\ 0 \\ 0 \end{bmatrix} \quad (16)$$

$$a_d \cong 1 - \frac{TR_2}{L_2} \quad b_d \cong \frac{T}{L_2} \quad g_d \cong \frac{-T}{L_2}. \quad (16)$$

The output voltage in (13) can be given by

$$\begin{aligned} v_i(k+1) &= \mathbf{c}^T \mathbf{x}_1(k+1) \\ &= \alpha v_c(k) + \beta v_{inv}(k) + \gamma i_{inv}(k) + \delta i_g(k) + \phi d_g(k) \end{aligned} \quad (17)$$

$$Z(s)_H \equiv \frac{V_s(s)}{I_g(s)} = -\frac{L_1 L_2 C_f s^4 + C_f (L_1 R_2 + L_2 R_1) s^3 + (R_1 R_2 C_f + L_1 + L_2) s^2 + (R_1 + R_2 + K_p) s + K_I}{L_1 C_f s^3 + R_1 C_f s^2 + s}. \quad (6)$$

where

$$\begin{aligned}\alpha &= 1 - \frac{TR_c}{L_1} & \beta &= \frac{TR_c}{L_1} \\ \gamma &= R_c \left(1 - \frac{T(R_c + R_1)}{L_1} \right) + \frac{T}{C_f} \\ \delta &= -\frac{T}{C_f} - R_c \left(\frac{TR_c}{L_1} + 1 \right) & \phi &= TR_c.\end{aligned}$$

Then, the dynamics of $v_i(k)$ can be obtained as

$$v_i(k+1) = \alpha v_i(k) + \beta v_{\text{inv}}(k) + \bar{\gamma} i_{\text{inv}}(k) + \bar{\delta} i_g(k) + \phi d_g(k) \quad (18)$$

where

$$\bar{\gamma} = \frac{T}{C_f} - \frac{TR_c R_1}{L_1} \quad \bar{\delta} = -\frac{T}{C_f} - \frac{2TR_c^2}{L_1}.$$

The voltage dynamics in (18) relates v_i to the inverter voltage and network currents, which act as disturbances. Equation (18) indicates that the inverter voltage can be controlled to yield a desired intermediate voltage. The latter can be controlled to yield the desired grid-side current. By considering possible variation in system parameters, the disturbed dynamics in (18) can be written as

$$v_i(k+1) = \alpha_o v_i(k) + \beta_o v_{\text{inv}}(k) + w(k) \quad (19)$$

where $w(k)$ is the lump of uncertainties imposed on v_i dynamics, and the subscript “o” denotes the nominal value.

Similarly, the grid-side current dynamics is subjected to grid uncertainties, including grid-side parameter variation and grid-voltage disturbances; therefore, (14) can be written as

$$i_g(k+1) = a_{do} i_g(k) + b_{do} v_i(k) + g_{do} f_g(k) \quad (20)$$

where the subscript “o” denotes the nominal value and f_g is the lump of uncertainties imposed on i_g dynamics.

Equations (19) and (20) represent the power-circuit dynamics and facilitate robust control design.

Considering other physical constraints, the preceding model is subjected to the following limits. The load current is limited to the maximum continuous current of the inverter or to the maximum available current of the inverter in a limited short-time operation. Also, the load voltage is limited to the maximum available output voltage of the inverter depending on the dc-link voltage.

B. Predictive Current-Control Design

Equations (19) and (20) can be used to synthesize the inverter control voltage that yields a reference grid-side current in the sense of deadbeat control as follows:

$$v_{\text{inv}}(k) = \frac{1}{\beta_o} \{ v_i(k+1) - \alpha_o v_i(k) - w(k) \} \quad (21a)$$

$$v_i(k) = \frac{1}{b_{do}} \{ i_g(k+1) - a_{do} i_g(k) - g_{do} f_g(k) \} \quad (21b)$$

Equation (21), however, does not account for system delays, which are caused by the nature of the PWM inverter as a zero-order-hold and the computational delay. Such delays reduce the

stability margins, particularly when high feedback gains are used (e.g., deadbeat control). The control timing sequence of a practical digital current controller can be explained as follows. The k th cycle generated by the PWM generator starts the control process. The synchronous sampling process starts at the k th cycle. The calculation time of the control algorithm should end before the $(k+1)$ th cycle, and the command voltage is uploaded into the PWM generator just before the $(k+1)$ th cycle. During the $(k+1)$ th period of the control process, the control voltages calculated in the previous period are applied via the VSI. The resultant phase currents are sensed using the $(k+2)$ th interrupt. Usually, the controller bandwidth is reduced in order to account for practical system’s delays. This results in lower control accuracy and failure to achieve a transient-following controller. On the other hand, if the delay effect is appropriately compensated, the bandwidth criterion is relaxed. In fact, the compensation of the time delay significantly increases the current-controller bandwidth without increasing the inverter’s switching frequency.

In order to enhance the bandwidth characteristics, in the presence of system delays, a delay compensation method is proposed in this paper. The compensation method adopts a natural observer and utilizes the predictive nature of the outputs of the internal-model generator (described in Section III-C) to force the delay element to be equivalently placed outside the close-loop control system. Hence, its effect on the closed-loop stability is eliminated, and the current controller can be designed with high-bandwidth characteristics.

During the $(k+1)$ th period of the control process, the current is forced by the control voltage at $(k+1)$ which is calculated in the k th period. The resultant current, which is sensed at the beginning of the $(k+2)$ th period, can be given by

$$i_g(k+2) = a_{do} i_g(k+1) + b_{do} v_i(k+1) + g_{do} f_g(k+1). \quad (22)$$

The grid-side current at $(k+2)$ is affected by the grid-side current at $(k+1)$ and the intermediate voltage at $(k+1)$. Accordingly, the grid-side current at $(k+2)$ can be given by

$$\begin{aligned}i_g(k+2) &= a_{do} (a_{do} i_g(k) + b_{do} v_i(k) + g_{do} f_g(k)) \\ &\quad + b_{do} (\alpha_o v_i(k) + \beta_o v_{\text{inv}}(k) + w(k)) \\ &\quad + g_{do} f_g(k+1).\end{aligned} \quad (23)$$

For current regulation, the grid-side current at $(k+2)$ can be regarded as the reference. Accordingly, the appropriate control voltage can be predictably obtained as follows:

$$\begin{aligned}v_{\text{inv}}^*(k+1) &= \frac{1}{\beta_o b_{do}} \{ i_g^*(k+2) - a_{do}^2 i_g(k) \\ &\quad - (a_{do} + \alpha_o) b_{do} v_i(k) \\ &\quad - a_{do} g_{do} f_g(k) - b_{do} w(k) - g_{do} f_g(k+1) \}\end{aligned} \quad (24)$$

where the superscript “*” denotes the reference value.

According to (24), the control voltage can be calculated with the measured quantities at the k th sample and the current and predicted internal-model dynamics, $w(k)$ and $f_g(k+1)$,

respectively. Therefore, the delay is equivalently removed outside the closed-loop control to appear in the two-step-ahead reference vector.

Under the assumption of known internal-model dynamics f_g and w , and by using (24) with the power-circuit dynamics in (19) and (20), the grid-side current can be given as

$$i_g(k) = i_g^*(k-2). \quad (25)$$

Accordingly, the frequency response of the reference-to-output transfer function is

$$G(e^{j\omega T}) = e^{-2j\omega T} \quad (26)$$

which has a unity gain and a phase lag corresponding to the two-sampling-period delay, which are equivalently removed outside the closed loop to appear in the reference side. To compensate for this delay, the forward estimate of the reference current is necessary. This equivalently works as adding an equal and opposite phase shift to the reference trajectory. Based on real-time analysis, a two-step forward prediction provides the necessary phase advance to minimize the steady-state error. As a result, the reference current is predicted as follows:

$$i_g^*(k+2) = 3i_g^*(k) - 2i_g^*(k-1). \quad (27)$$

Unlike conventional deadbeat controllers, where the counter voltage is usually measured or estimated by linear extrapolations [21] or assuming it is constant over two or three sampling periods [22], the proposed controller utilizes the one-step-ahead disturbance voltage $f_g(k+1)$, which can be robustly predicted by the adaptive internal-model generator described in the following section. The utilization of the estimated internal-model dynamics provides efficient means for control-effort energy shaping and provides the necessary phase advance of the estimated disturbance, which compensates for the total system's delay.

C. Internal-Model Generation for Robust Active Damping and Current Control

To ensure high disturbance rejection of grid distortion, converter resonance, and parametric instabilities, an adaptive internal model for unknown dynamics w and f_g is proposed and emerged in the control structure. Due to the periodic time-varying nature of the grid voltage, harmonics, unbalance, and other uncertainties, the internal-model generator utilizes a NN-based adaptation algorithm that works as a real-time optimization agent.

Relying on the simplified system model given by (19) and (20), a simple two-layer NN-based adaptive observer with the following input/output relation can be constructed:

$$\begin{bmatrix} \hat{v}_i(k) \\ \hat{i}_g(k) \end{bmatrix} = \mathbf{F}_o \begin{bmatrix} v_i(k-1) \\ i_g(k-1) \end{bmatrix} + \mathbf{H}_o \begin{bmatrix} v_{\text{inv}}(k-1) \\ v_i(k-1) \end{bmatrix} + \mathbf{M}_o \begin{bmatrix} \hat{w}(k-1) \\ \hat{f}_g(k-1) \end{bmatrix} \quad (28)$$

where

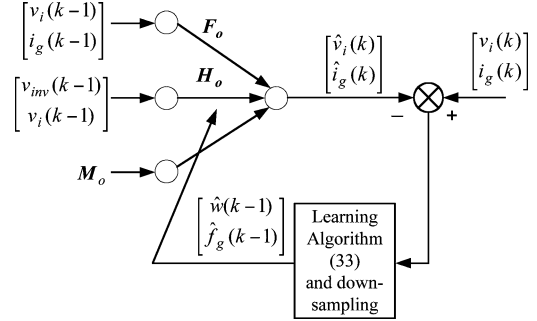


Fig. 4. Network structure of the NN-based internal-model generator.

$\mathbf{F}_o = \begin{bmatrix} \alpha_o & 0 \\ 0 & a_{do} \end{bmatrix}$ $\mathbf{H}_o = \begin{bmatrix} \beta_o & 0 \\ 0 & b_{do} \end{bmatrix}$ $\mathbf{M}_o = \begin{bmatrix} 1 & 0 \\ 0 & g_{do} \end{bmatrix}$. and $\begin{bmatrix} \hat{v}_i(k) \\ \hat{i}_g(k) \end{bmatrix}$ is the output of the NN adaptive observer, and the symbol “ $\hat{\cdot}$ ” denotes the estimated quantity.

Fig. 4 depicts the network structure of the NN adaptive observer.

Under the same input voltage and disturbance, the estimated voltage approaches the actual one, even though the NN-based observer in (28) has an open-loop structure. Therefore, convergence of the proposed observer can be achieved with an appropriate disturbance adaptation using the estimation error

$$\begin{bmatrix} e_v(k) \\ e_i(k) \end{bmatrix} \equiv \begin{bmatrix} v_i(k) \\ i_g(k) \end{bmatrix} - \begin{bmatrix} \hat{v}_i(k) \\ \hat{i}_g(k) \end{bmatrix}. \quad (29)$$

Due to the properties of guaranteed convergence, and optimizing the performance, a discrete-type quadratic error function is defined as follows:

$$E(k) = \frac{1}{2} (e_v(k)^2 + e_i(k)^2). \quad (30)$$

The disturbance voltage can be adaptively estimated by minimizing the error function $E(k)$ by performing the steepest descent method on a surface in $[\hat{w} \ \hat{f}_g]^T$ space, where its height is equal to the measured error. In order to minimize the error function $E(k)$, one can evaluate the following Jacobian:

$$\mathbf{J} = \begin{bmatrix} \frac{\partial E}{\partial \hat{w}} \\ \frac{\partial E}{\partial \hat{f}_g} \end{bmatrix} = \begin{bmatrix} \frac{\partial E}{\partial \hat{v}_i} \frac{\partial \hat{v}_i}{\partial \hat{w}} \\ \frac{\partial E}{\partial \hat{i}_g} \frac{\partial \hat{i}_g}{\partial \hat{f}_g} \end{bmatrix} \quad (31)$$

The right-hand side term of (31) can be evaluated as

$$\mathbf{J} = -\mathbf{M}_o \left\{ \begin{bmatrix} v_i(k) \\ i_g(k) \end{bmatrix} - \begin{bmatrix} \hat{v}_i(k) \\ \hat{i}_g(k) \end{bmatrix} \right\}. \quad (32)$$

For the steepest descent algorithm, the change in the weight is calculated as

$$\begin{aligned} \begin{bmatrix} \hat{w}(k+1) \\ \hat{f}_g(k+1) \end{bmatrix} &= \begin{bmatrix} \hat{w}(k) \\ \hat{f}_g(k) \end{bmatrix} + \begin{bmatrix} \Delta \hat{w}(k) \\ \Delta \hat{f}_g(k) \end{bmatrix} = \begin{bmatrix} \hat{w}(k) \\ \hat{f}_g(k) \end{bmatrix} - \eta \mathbf{J} \\ &= \begin{bmatrix} \hat{w}(k) \\ \hat{f}_g(k) \end{bmatrix} + \eta \mathbf{M}_o \left\{ \begin{bmatrix} v_i(k) \\ i_g(k) \end{bmatrix} - \begin{bmatrix} \hat{v}_i(k) \\ \hat{i}_g(k) \end{bmatrix} \right\} \end{aligned} \quad (33)$$

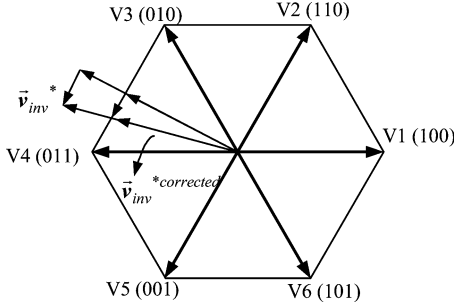


Fig. 5. Control voltage limit in the space vector plane.

where $\eta = \begin{bmatrix} \eta_v & 0 \\ 0 & \eta_i \end{bmatrix}$ is an adaptation gain matrix.

The adaptive estimation law in (33) provides a simple iterative gradient algorithm designed to minimize (30). As a result, the estimate can be reliably used to embed an internal model for the uncertainty function within the current-feedback structure, resulting in equivalent control to cancel the power-circuit disturbances. Therefore, the estimated internal-model dynamics can be used to robustly calculate the control voltage as follows:

$$\begin{aligned} v_{\text{inv}}^*(k+1) = & \frac{1}{\beta_o b_{do}} \{ i_g^*(k+2) - a_{do}^2 i_g(k) \\ & - (a_{do} + \alpha_o) b_{do} v_i(k) \\ & - a_{do} g_{do} \hat{f}_g(k) - b_{do} \hat{w}(k) - g_{do} \hat{f}_g(k+1) \}. \end{aligned} \quad (34)$$

The control law in (34) can be easily tuned using nominal system parameters and it can be synthesized using a PWM technique.

Since the reference current vector is generated in the synchronous reference frame, the effect of the synchronous frame rotation should be considered to minimize the phase lag in the injected current. With the aforementioned control sequence, the synchronous-frame rotates, and there will be a position difference between the k th and the $(k+1)$ th interrupt times. Since the control voltage is applied during the $(k+1)$ th period, the position difference can be adjusted by averaging the reference frame position over one switching period. Therefore, the corrected voltage command can be given in the following space vector form:

$$\vec{v}_{\text{inv}}^*(k+1) = \vec{v}_{\text{inv}}^*(k+1) e^{j(2.5\theta(k)-1.5\theta(k-1))} \quad (35)$$

where $\theta(k)$ is the synchronous frame position at the current-sampling period.

To achieve higher dc-link voltage utilization and lower distortion in the output current, the space vector modulation (SVM) technique can be employed to synthesize the control voltage in (34). The control-voltage-limit method utilizes the space vector voltage limit in the same direction of the reference voltage as shown in Fig. 5.

D. Convergence Analysis

The proposed control scheme can be treated as a two-DOF predictive control system, composed of a predictive current con-

troller and an internal-model controller. Among the merits of this design is that both controllers can be analyzed independently [23].

First, this section analyzes the stability of the internal-model controller and provides a guideline in tuning the controller parameters in the sense of Lyapunov functions. The Lyapunov function is selected as

$$V_T(e_v(k), e_i(k), k) = \frac{1}{2} (e_v(k)^2 + e_i(k)^2). \quad (36)$$

The Lyapunov's convergence criterion must be satisfied such that

$$V_T(k) \Delta V_T(k) < 0 \quad (37)$$

where $\Delta V_T(k)$ is the change in the total Lyapunov function.

The stability condition in (37) is satisfied when $\Delta V_T(k) < 0$, as $V_T(k)$ is defined as an arbitrary positive as shown in (36).

The change in the Lyapunov function is given by

$$\Delta V_T(k) = V_T(e_v(k+1), e_i(k+1)) - V_T(e_v(k), e_i(k)) < 0. \quad (38)$$

Since the estimated internal-model dynamics can be assumed to be naturally continuous, the change in the error $\Delta e_v(k)$ and $\Delta e_i(k)$ due to the adaptation process of the NN internal-model generator can be given by

$$\begin{aligned} \begin{bmatrix} \Delta e_v(k) \\ \Delta e_i(k) \end{bmatrix} &= \begin{bmatrix} e_v(k+1) - e_v(k) \\ e_i(k+1) - e_i(k) \end{bmatrix} = \begin{bmatrix} \frac{\partial e_v(k)}{\partial \hat{w}} \Delta \hat{w}(k) \\ \frac{\partial e_i(k)}{\partial \hat{f}_g} \Delta \hat{f}_g(k) \end{bmatrix} \\ &= \begin{bmatrix} \eta_v & 0 \\ 0 & \eta_i \end{bmatrix} \begin{bmatrix} \frac{\partial e_v(k)}{\partial \hat{w}} \frac{\partial \hat{v}_i(k)}{\partial \hat{w}} e_v(k) \\ \frac{\partial e_i(k)}{\partial \hat{f}_g} \frac{\partial \hat{i}_g(k)}{\partial \hat{f}_g} e_i(k) \end{bmatrix}. \end{aligned} \quad (39)$$

By substituting (39) in (38), $\Delta V_T(k)$ can be represented as

$$\begin{aligned} \Delta V_T(k) &= e_v(k) \Delta e_v(k) + e_i(k) \Delta e_i(k) \\ &\quad + \frac{1}{2} (\Delta e_v(k)^2 + \Delta e_i(k)^2) \\ &= \eta_v \frac{\partial e_v(k)}{\partial \hat{w}} \frac{\partial \hat{v}_i(k)}{\partial \hat{w}} e_v(k)^2 + \eta_i \frac{\partial e_i(k)}{\partial \hat{f}_g} \frac{\partial \hat{i}_g(k)}{\partial \hat{f}_g} e_i(k)^2 \\ &\quad + \frac{\eta_v^2}{2} \left\| \frac{\partial e_v(k)}{\partial \hat{w}} \right\|^2 \left\| \frac{\partial \hat{v}_i(k)}{\partial \hat{w}} \right\|^2 e_v(k)^2 \\ &\quad + \frac{\eta_i^2}{2} \left\| \frac{\partial e_i(k)}{\partial \hat{f}_g} \right\|^2 \left\| \frac{\partial \hat{i}_g(k)}{\partial \hat{f}_g} \right\|^2 e_i(k)^2 \end{aligned} \quad (40)$$

where $\|\cdot\|$ is the Euclidean norm in \mathbb{R}^n .

Since $\frac{\partial \hat{v}_i(k)}{\partial \hat{w}} = -\frac{\partial e_v(k)}{\partial \hat{w}}$ and $\frac{\partial \hat{i}_g(k)}{\partial \hat{f}_g} = -\frac{\partial e_i(k)}{\partial \hat{f}_g}$, then (40) can be given by

$$\begin{aligned}\Delta V_T(k) = & - \left\{ \eta_v \left\| \frac{\partial \hat{v}_i(k)}{\partial \hat{w}} \right\|^2 - \frac{\eta_v^2}{2} \left\| \frac{\partial \hat{v}_i(k)}{\partial \hat{w}} \right\|^4 \right\} e_v(k)^2 \\ & - \left\{ \eta_i \left\| \frac{\partial \hat{i}_g(k)}{\partial \hat{f}_g} \right\|^2 - \frac{\eta_i^2}{2} \left\| \frac{\partial \hat{i}_g(k)}{\partial \hat{f}_g} \right\|^4 \right\} e_i(k)^2.\end{aligned}\quad (41)$$

To satisfy the stability condition in (37), the adaptation gains are chosen as

$$0 < \eta_v < \frac{2}{\max_k [\|\partial \hat{v}_i(k)/\partial \hat{w}\|^2]} \text{ or } 0 < \eta_v < 2 \quad (42a)$$

$$0 < \eta_i < \frac{2}{\max_k [\|\partial \hat{i}_g(k)/\partial \hat{f}_g\|^2]} \text{ or } 0 < \eta_i < \frac{2}{g_{do}^2}. \quad (42b)$$

Using the aforementioned condition, it can be seen that $\Delta V_T(k) < 0$, and it follows that the adaptation error is monotonically nonincreasing. Therefore, the convergence is guaranteed, i.e., $\begin{bmatrix} \tilde{w}(k) \\ \tilde{f}_g(k) \end{bmatrix}$ and $\begin{bmatrix} e_v(k) \\ e_i(k) \end{bmatrix} \rightarrow 0$ and as $k \rightarrow \infty$, where $\begin{bmatrix} \tilde{w}(k) \\ \tilde{f}_g(k) \end{bmatrix} = \begin{bmatrix} w(k) \\ f_g(k) \end{bmatrix} - \begin{bmatrix} \hat{w}(k) \\ \hat{f}_g(k) \end{bmatrix}$ is the internal-model estimation error vector.

Second, the stability and robustness of the predictive control scheme can be analyzed by considering the discrete-time current dynamics and the robust control law in (34).

$$\begin{aligned}i_g(k+2) &= a_{do}^2 i_g(k) + (a_{do} + \alpha_o) b_{do} v_i(k) + a_{do} g_{do} f_g(k) \\ &\quad + \beta_o b_{do} v_{inv}(k) + b_{do} w(k) + g_{do} f_g(k+1) \\ &= a_{do}^2 i_g(k) + (a_{do} + \alpha_o) b_{do} v_i(k) + a_{do} g_{do} f_g(k) \\ &\quad + i_g^*(k+2) - a_{do}^2 i_g(k) - (a_{do} + \alpha_o) b_{do} v_i(k) \\ &\quad - a_{do} g_{do} \hat{f}_g(k) - b_{do} \hat{w}(k) - g_{do} \hat{f}_g(k+1) \\ &\quad + b_{do} w(k) + g_{do} f_g(k+1) \\ &= i_g^*(k+2) + a_{do} g_{do} \tilde{f}_g(k) + b_{do} \hat{w}(k) + g_{do} \tilde{f}_g(k+1).\end{aligned}\quad (43)$$

Then, the tracking error can be obtained as follows:

$$\begin{aligned}i_g^*(k+2) - i_g(k+2) \\ = -a_{do} g_{do} \tilde{f}_g(k) - b_{do} \hat{w}(k) - g_{do} \tilde{f}_g(k+1)\end{aligned}\quad (44)$$

or

$$\begin{aligned}i_g^*(k) - i_g(k) \\ = -a_{do} g_{do} \tilde{f}_g(k-2) - b_{do} \hat{w}(k-2) - g_{do} \tilde{f}_g(k-1).\end{aligned}\quad (45)$$

As seen in (45), the current-tracking error is proportional to the uncertainty estimation error. With the steepest descent algorithm in (33), the convergence of the observation and internal-model generation is guaranteed. Therefore, $i_g^*(k) - i_g(k) \rightarrow 0$, as $k \rightarrow \infty$.

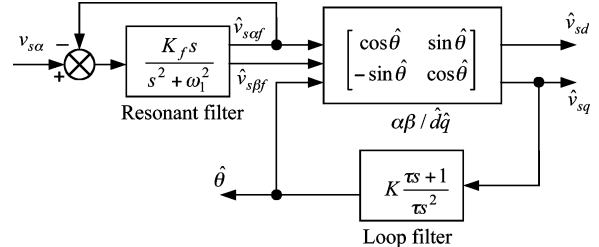


Fig. 6. Robust PLL algorithm.

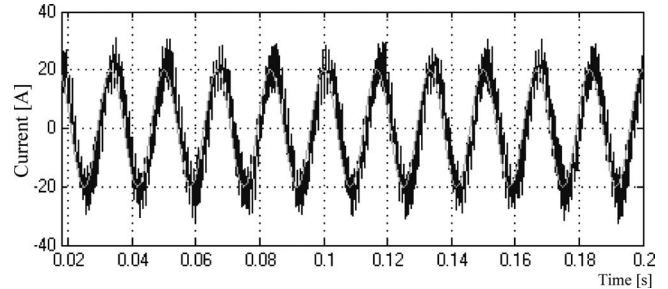


Fig. 7. Control performance of the PI controller: harmonic resonance at 17th harmonic with 40% mismatch in the grid inductance.

E. Synchronization

Smooth and accurate information of the position of the grid-voltage vector is necessary to guarantee high-power-quality injection even under the presence of grid-voltage harmonics, unbalance, and voltage disturbances. To achieve this objective, a simple and robust synchronization method is adopted. The method utilizes a dq -PLL with a resonant filter tuned at the fundamental grid frequency. The utilization of resonant filters in the synchronization problem provides high attenuation for the frequency modes to be eliminated from the controlled tracking error. In addition, the states of a second-order resonant filter are in quadrature. This feature enables the utilization of only one filter for both voltage components in the stationary reference-frame, hence, yielding a computationally efficient solution. Fig. 6 shows the configuration of the resonant-filter-based dq -PLL algorithm, where K_f is the gain of the resonant filter, ω_1 is the resonant frequency, $\hat{v}_{s\alpha f}$ and $\hat{v}_{s\beta f}$ are the filtered estimates of the $\alpha\beta$ -components of the grid voltage, respectively, K and τ are the loop filter parameters, and $\hat{\theta}$ is the estimated grid-voltage vector angle. The loop filter parameters could be chosen to achieve predefined time-response characteristics in the sense of a standard second-order system.

IV. EXPERIMENTAL RESULTS

To evaluate the performance of the proposed control scheme, a three-phase grid-connected PWM VSI system incorporated with the proposed control scheme, as reported in Fig. 3, has been used. The system parameters are as follows: grid phase voltage = 120 V at 60 Hz, nominal dc-link voltage = 400 V, nominal parameters $L_1 = 0.8 \text{ mH}$, $R_1 = 0.2 \Omega$, $L_2 = 0.2 \text{ mH}$ (stiff grid), $L_2 = 6.0 \text{ mH}$ (weak grid), $R_2 = 0.2 \Omega$, and $C_f = 40 \mu\text{F}$.

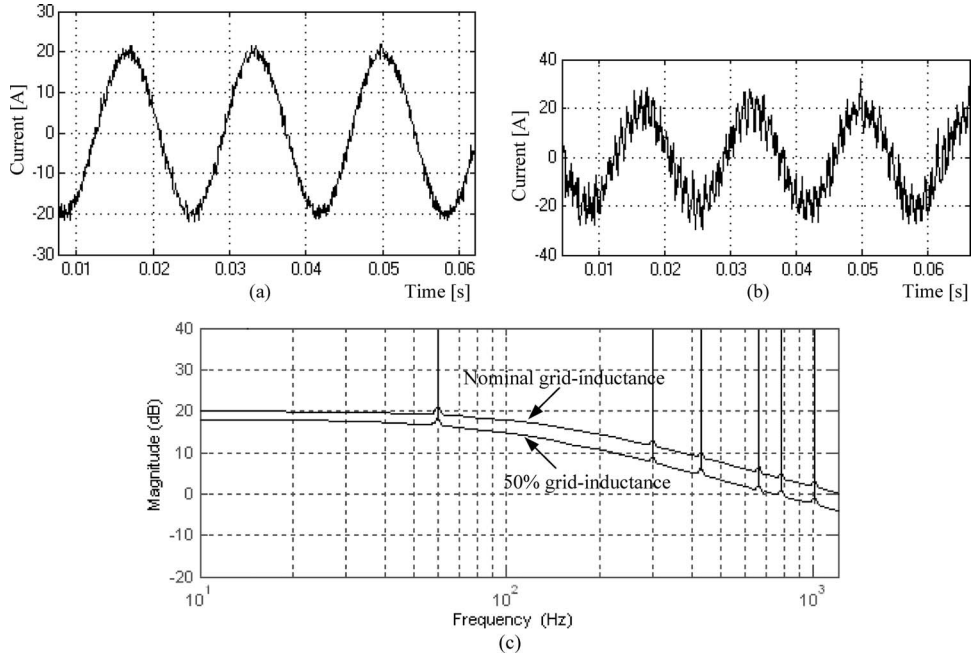


Fig. 8. Performance of the P-HRES controller. (a) Current-control performance at nominal parameters. (b) Current-control performance with 50% mismatch in the grid inductance. (c) Frequency characteristics of the P-HRES controller at nominal and uncertain grid inductance.

The real-time code of the proposed control scheme is generated by the Real-Time WorkShop, under MATLAB/Simulink environment. The TMS320F28335 DSP has been chosen as an embedded platform for experimental validation with switching frequency of 8 kHz. Since the sharp insulated-gate bipolar transistor commutation spikes may impair the current acquisition process, the synchronous sampling technique with a symmetric SVM module is adopted. With this method, the sampling is performed at the beginning of each modulation cycle. Only two phases current are fed back, as the neutral is isolated.

To verify the feasibility of the proposed controller, different operating conditions have been considered. For the purpose of performance comparison, the proposed control scheme is compared to the following current controllers:

- 1) conventional PI current controller;
- 2) P-HRES [4];
- 3) predictive controller [24];
- 4) proposed controller.

The controllers under comparison are tested under the following grid-distortion conditions—grid-voltage harmonics: 3% 5th harmonic, 2% 7th harmonic, 1% 11th harmonic, 1% 13th harmonic, and 0.5% 17th harmonics; grid-voltage unbalance: 7% voltage unbalance factor.

In the examined controllers, the magnitude of the current command is set at 20 A with unity power factor for $t \geq 0.0167$ s.

First, to show the effect of harmonic resonance at parameter variation with conventional PI current control, only the 17th harmonic is included in the grid distortion. Further, the grid inductance is increased by 40% of its nominal value. The mismatch in the grid inductance remarkably shifts the resonance

frequency of the power circuit to be around 1.0 kHz, which can be easily excited by the 17th harmonic grid distortion. The harmonic resonance can be seen in the current waveform of Fig. 7.

Second, to enhance the disturbance rejection performance, the P-HRES controller [4] is adopted. The controller provides internal-model dynamics at selected harmonic frequencies. Fig. 8(a) shows the control performance of the P-HRES controller with harmonic compensators tuned at the fundamental, 5th, 7th, 11th, 13th, and 17th harmonics at nominal system parameters. The current quality is improved due to the presence of internal models that are tuned at specific distortion modes. Fig. 8(b) shows the control performance of the P-HRES controller with harmonic compensators tuned at the fundamental, 5th, 7th, 11th, 13th, and 17th harmonics, and 50% mismatch in the grid inductance. The mismatch in the grid inductance shifts the effective open-loop bandwidth of the P-HRES controller and leads to current-control instability, as shown in Fig. 8(b). Fig. 8(c) shows the frequency characteristics of the open-loop P-HRES controller at nominal grid inductance and 50% grid inductance. In the latter case, the resonant mode of the 17th harmonic lies outside the reduced bandwidth leading to sustained oscillations in the output current. These oscillations and the poor dynamic response are indeed the result of the instability of the control system. The current-control limits and overmodulation of the PWM limit the magnitude of these oscillations (limit cycles). Active-damping control can mitigate such instability; however, the active-damping controller should be tuned at a specified grid inductance or power-circuit parameters in general. The effectiveness of the active-damping control is lost even with small uncertainty in system parameters, which leads

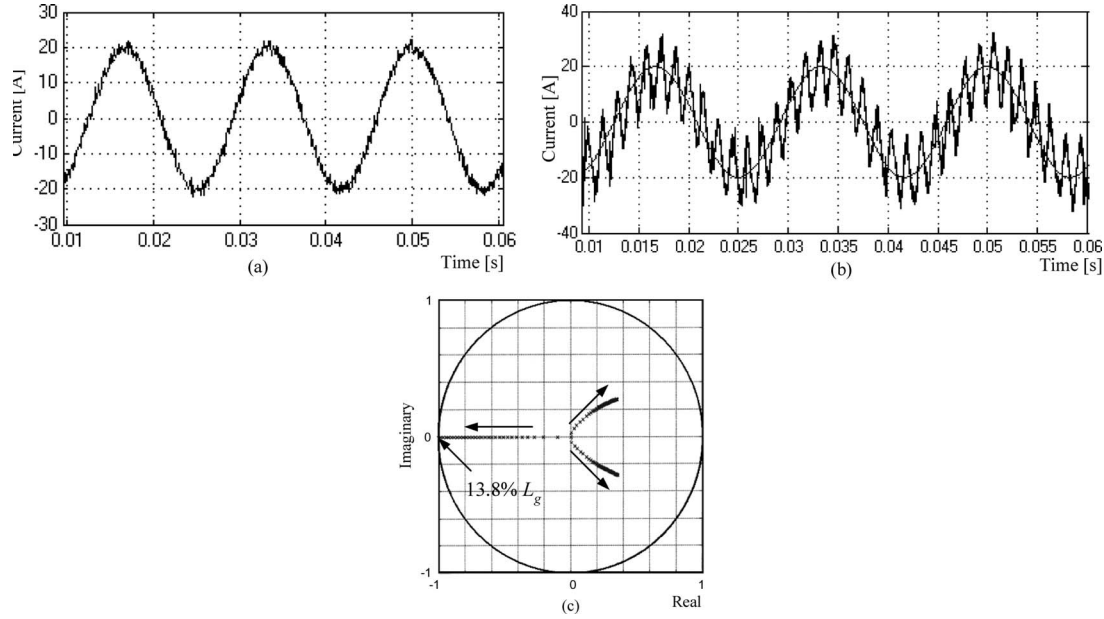


Fig. 9. Performance of the predictive controller. (a) Current-control performance at nominal parameters. (b) Current-control performance with 30% mismatch in the grid inductance. (c) Root locus of the current-control dynamics with the grid inductance as a parameter.

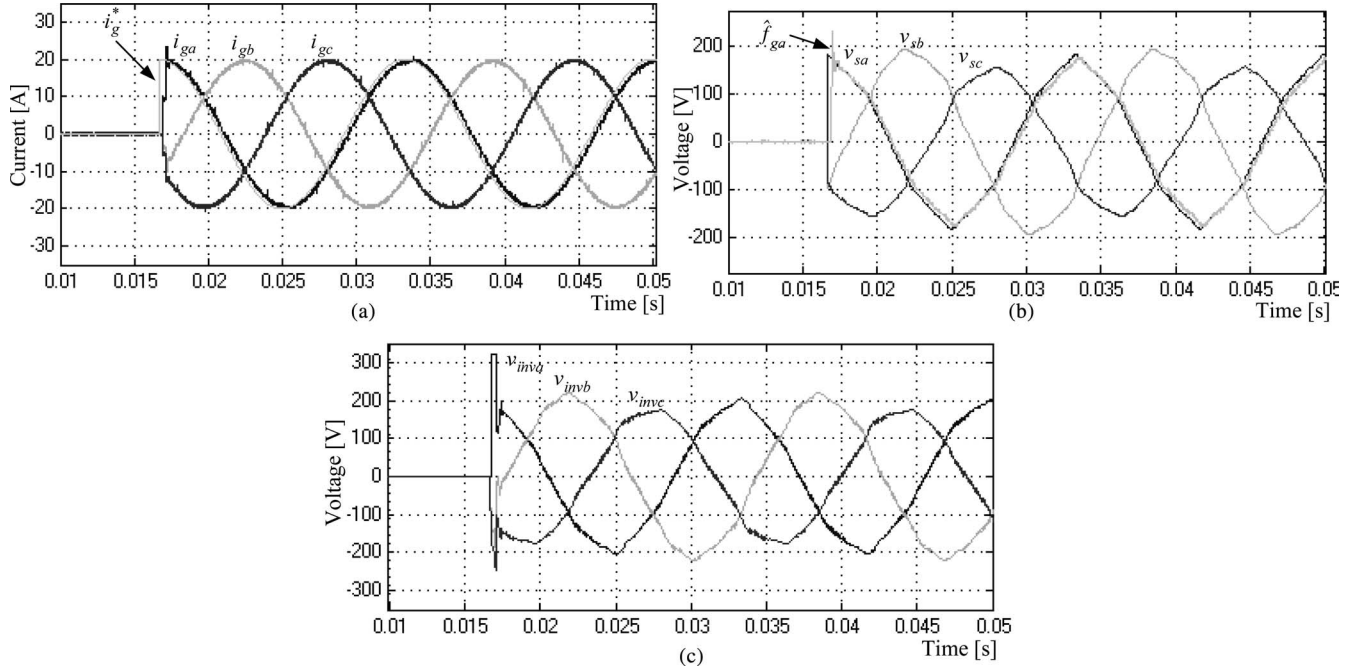


Fig. 10. Dynamic performance and the grid-distortion rejection ability of the proposed controller. (a) Reference and injected gird currents. (b) Grid voltage and estimated gird-side uncertainty function. (c) Inverter control voltage.

to a remarkable shift in the resonance frequency of the power circuit [4].

Third, the performance of the predictive current controller [24] is evaluated. Fig. 9(a) shows the control performance of the predictive controller under nominal system parameters. Fig. 9(b) shows the control performance of the same controller with 30% mismatch of the grid inductance. The robustness of the conventional predictive controller is an issue

in grid-connected converter applications. Fig. 9(c) shows the root locus of the current-control dynamics with predictive control and with the grid inductance as a parameter. The dominant pole becomes marginally stable with approximately 13.8% mismatch in the grid inductance. The instability of the current-control loop at parameter variation along with the saturation effect of the current-control loop and the modulator lead to sustained oscillations in the current response, as shown in

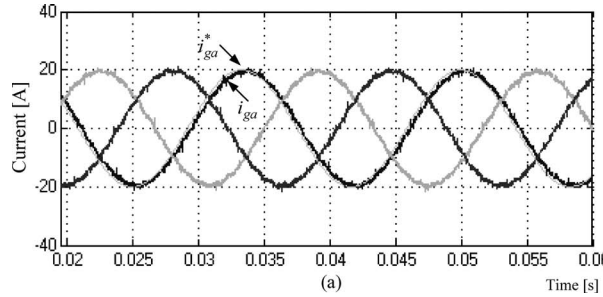


Fig. 11. Active-damping performance of the proposed controller with 17th grid harmonic and 40% mismatch in the grid inductance. (a) Reference and injected grid currents. (b) Inverter control voltage.

Fig. 9(b). It should be noted that the proposed current controller is a predictive deadbeat controller with improved robustness against uncertainties in system parameters and background grid distortion.

Fourth, the proposed control scheme is evaluated. The proposed controller is tuned using nominal system parameters $\eta_v = 1$ and $\eta_i = 40$. The adaptation gains are selected according to the stability bounds derived in (42) to yield fast and stable estimates. Since the proposed control structure relies on embedding the frequency modes of the grid harmonics and disturbances through the closed-loop current controller, the current controller mainly handles the tracking task, whereas the regulation performance is mainly realized through uncertainty estimation and compensation control. Fig. 10 shows the control performance of the proposed controller. Fig. 10(a) shows that high power-quality current injection, with a total harmonic distortion of 0.96%, is yielded with the proposed current-control scheme. This result meets the grid-connection standards [25]. The high-quality current injection is the natural result of the high disturbance rejection ability of the proposed current controller. Fig. 10(b) shows the actual distorted and unbalanced grid voltages and the estimated uncertainty functions, which closely track the actual grid voltage. Fig. 10(c) shows the inverter control voltage. The uncertainty modes can be effectively embedded in the control effort to cancel the effect of grid-voltage harmonics and unbalance.

To show the robustness of the proposed controller against harmonic resonance at parameter variation, only the 17th harmonic is included in the grid distortion. Further, the grid inductance is increased by 40%. The mismatch in the grid inductance remarkably shifts the resonance frequency of the power circuit to be around 1.0 kHz, which can be easily excited by the 17th harmonic grid distortion; however, the estimated internal-model dynamics, which include any deviation from the nominal model, inserts the necessary active damping and control-signal energy shaping to mitigate such harmonic resonance under uncertain conditions. Fig. 11(a) shows the current-control performance in this case, whereas Fig. 11(b) shows the corresponding inverter control voltage. It can be also noted that the high-bandwidth predictive current controller enables such energy-shaping control at relatively high frequencies.

For further performance evaluation of the proposed internal-model estimator, the effect of sudden grid-voltage disturbance and phase jump is considered. Fig. 12(a) shows the estimator

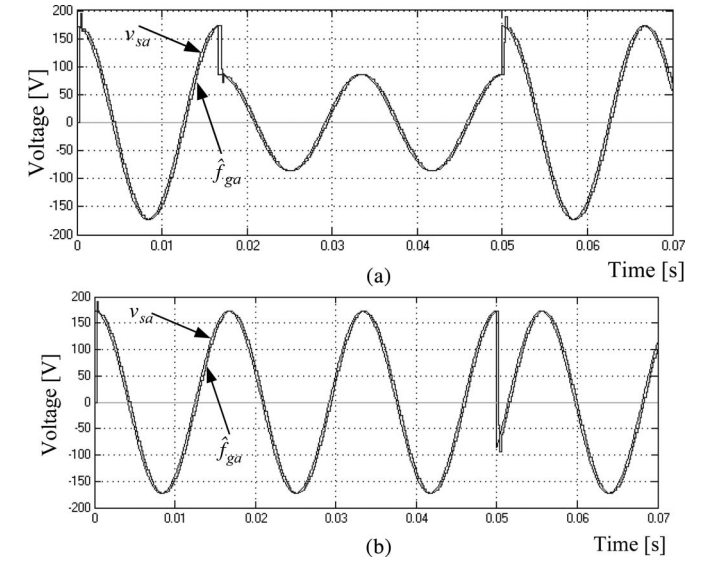
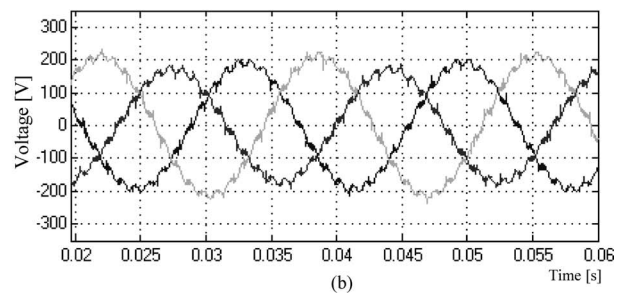


Fig. 12. Estimator performance at (a) sudden voltage dip and (b) sudden phase jump.

performance with a 50% sudden change in the grid voltage, whereas Fig. 12(b) shows the estimator performance with a sudden phase jump in the grid voltage at $t = 0.05$ s. The proposed uncertainty estimation algorithm provides fast convergence properties, and it can track grid-voltage disturbances with a relatively high-bandwidth. It should be noted that the active-damping performance of the converter resonance is inherently achieved by the decoupled power-circuit control concept [based on the model in (19) and (20), which can be treated as a multiloop active-damping control model], whereas the robustness against converter resonance at parameter variation is achieved by internal-model generation.

Table I summarizes the main features of the compared controllers. The reported results indicate that the proposed scheme results in robust current tracking and regulation responses, even under the occurrence of large uncertainties in system parameters and background distortion.

V. CONCLUSION

A robust interfacing scheme for DG inverters featuring robust mitigation of converter-grid resonance, grid-induced distortion,

TABLE I
PERFORMANCE FEATURES OF COMPARED CONTROLLERS

Controllers	Main features
Conventional PI controller	<ul style="list-style-type: none"> - Simple structure - Very weak rejection of grid-induced distortion - Possible grid-converter resonance - Current control instability at parameter variation
- Proportional resonant controller (P-RES) [8]	<ul style="list-style-type: none"> - Simple structure - Strong trade-off between stability and rejection of grid-induced distortion - Possible grid-converter resonance - Current control instability at parameter variation
- Proportional harmonic resonant controller (P-HRES) [4]	<ul style="list-style-type: none"> - Simple structure - Strong ability to reject grid-induced distortion - Possible grid-converter resonance - Current control instability at parameter variation
- Predictive controller [24]	<ul style="list-style-type: none"> - Modest structure - Strong ability to reject grid-induced distortion at pre-set modes - Possible grid-converter resonance - Current control instability at parameter variation
- Proposed controller	<ul style="list-style-type: none"> - Modest structure - Strong ability to reject grid-induced distortion - Active damping of grid-converter resonance at parameter variation - Current control stability at parameter variation - Adaptive nature that facilitates plug-and-play integration under different grid conditions

and parametric instabilities has been introduced. The proposed scheme relies on a high-bandwidth current-control loop, which is designed with continuous wideband active damping against converter-grid disturbances and parametric uncertainties by providing adaptive internal-model dynamics. Theoretical analysis and comparative experimental results have been presented to demonstrate the effectiveness of the proposed control scheme. The reported results indicate that the proposed control scheme yields a stable and high-power-quality current-control performance under the challenging uncertain nature of distribution systems and practical system constraints. Therefore, it can be used to facilitate plug-and-play integration of inverter-based DG into existing distribution systems; hence increasing the system penetration of DG.

REFERENCES

- [1] F. Z. Peng, "Special issue on distributed power generation," *IEEE Trans. Power Electron.*, vol. 19, no. 5, pp. 1157–1158, Sep. 2004.
- [2] F. Blaabjerg, Z. Chen, and S. B. Kjaer, "Power electronics as efficient interface in dispersed power generation systems," *IEEE Trans. Power Electron.*, vol. 19, no. 5, pp. 1184–1194, Sep. 2004.
- [3] H. Bindner and P. Lundsager, "Integration of wind power in the power system," in *Proc. IEEE Ind. Electron. Soc. Conf. IECON 2002*, Nov., vol. 4, pp. 3309–3316.
- [4] M. Liserre, R. Teodorescu, and F. Blaabjerg, "Stability of photovoltaic and wind turbine grid-connected inverters for a large set of grid impedance values," *IEEE Trans. Power Electron.*, vol. 21, no. 1, pp. 263–272, Jan. 2006.
- [5] F. Blaabjerg, R. Teodorescu, M. Liserre, and A. V. Timbus, "Overview of control and grid synchronization for distributed power generation systems," *IEEE Trans. Ind. Electron.*, vol. 53, no. 5, pp. 1398–1409, Oct. 2006.
- [6] M. Calais, J. Myrzik, T. Spooner, and V. G. Agelidis, "Inverters for single-phase grid connected photovoltaic systems—An overview," in *Proc. IEEE Power Electron. Spec. Conf. (PESC2002)*, pp. 1995–2000.
- [7] Y. A.-R. I. Mohamed and E. F. El-Saadany, "Robust high-bandwidth discrete-time predictive current control with predictive internal model—A unified approach for voltage-source PWM converters," *IEEE Trans. Power Electron.*, vol. 23, no. 1, pp. 126–136, Jan. 2008.
- [8] E. Twinning and D. G. Holmes, "Grid current regulation of a three-phase voltage source inverter with an LCL input filter," *IEEE Trans. Power Electron.*, vol. 18, no. 3, pp. 888–895, May 2003.
- [9] E. Twinning, "Modeling grid-connected voltage source inverter operation," in *Proc. AUPEC2001*, pp. 501–506.
- [10] M. Bollen, P. Ribeiro, E. Larsson, and C. Lundmark, "Limits for voltage distortion in frequency range 2 to 9 kHz," *IEEE Trans. Power Del.*, vol. 23, no. 3, pp. 1481–1487, Jul. 2008.
- [11] M. Liserre, R. Teodorescu, and F. Blaabjerg, "Multiple harmonics control for three-phase grid converter systems with the use of PI-RES current controller in a rotating frame," *IEEE Trans. Power Electron.*, vol. 21, no. 3, pp. 836–841, May 2006.
- [12] M. Liserre, A. Dell'Aquila, and F. Blaabjerg, "Genetic algorithm-based design of the active damping for an LCL-filter three-phase active rectifier," *IEEE Trans. Power Electron.*, vol. 19, no. 1, pp. 76–86, Jan. 2004.
- [13] G. Shen, D. Xu, L. Cao, and X. Zhu, "An improved control strategy for grid-connected voltage source inverter with LCL filer," *IEEE Trans. Power Electron.*, vol. 23, no. 4, pp. 1899–1906, Jul. 2008.
- [14] J. Dannehl, F. W. Fuchs, S. Hansen, and P. B. Thogersen, "Investigation of active damping approaches for PI-based current control of grid-connected PWM converters with LCL filters," in *Proc. IEEE Energy Convers. Congr. Expo., ECCE 2009*, pp. 2998–3005.
- [15] I. J. Gabe, V. F. Montagner, and H. Pinheiro, "Design and implementation of a robust current controller for VSI connected to the grid through an LCL filter," *IEEE Trans. Power Electron.*, vol. 24, no. 6, pp. 1444–1452, Jun. 2009.
- [16] J. Dannehl, F. W. Fuchs, and P. B. Thogersen, "PI state space current control of grid-connected PWM converters with LCL filters," *IEEE Trans. Power Electron.*, to be published.
- [17] B. K. Bose, "Neural network applications in power electronics and motor drives—An introduction and perspective," *IEEE Trans. Ind. Electron.*, vol. 54, no. 1, pp. 14–33, Feb. 2007.
- [18] K. S. Narendra and K. Parthasarathy, "Identification and control of dynamical systems using neural networks," *IEEE Trans. Neural Netw.*, vol. 1, no. 1, pp. 4–27, Jan. 1990.
- [19] J. R. Noriega and H. Wang, "A direct adaptive neural-network control for unknown nonlinear systems and its application," *IEEE Trans. Neural Netw.*, vol. 9, no. 1, pp. 27–34, Jan. 1998.
- [20] J. Dannehl, C. Wessels, and F. W. Fuchs, "Limitations of voltage-oriented PI current control of grid-connected PWM rectifiers with LCL filters," *IEEE Trans. Ind. Electron.*, vol. 56, no. 2, pp. 380–388, Feb. 2009.

- [21] G. H. Bode, P. C. Loh, M. J. Newman, and D. G. Holmes, "An improved robust predictive current regulation algorithm," *IEEE Trans. Ind. Appl.*, vol. 41, no. 6, pp. 1720–1733, Nov./Dec. 2005.
- [22] L. Malesani, P. Mattavelli, and S. Buso, "Robust dead-beat current control for PWM rectifiers and active filters," *IEEE Trans. Ind. Appl.*, vol. 35, no. 3, pp. 613–620, May/Jun. 1999.
- [23] J. W. Howze and S. P. Bhattacharyya, "Robust tracking, error feedback, and two-degree-of-freedom controllers," *IEEE Trans. Automat. Control*, vol. 42, no. 7, pp. 980–983, Jul. 1997.
- [24] A. Timbus, M. Liserre, R. Teodorescu, P. Rodriguez, and F. Blaabjerg, "Evaluation of current controllers for distributed power generation systems," *IEEE Trans. Power Electron.*, vol. 24, no. 3, pp. 654–664, Mar. 2009.
- [25] *IEEE Standard for Interconnecting Distributed Resources with Electric Power Systems*, IEEE Standard 1547-2003, Jul. 2003.

Yasser Abdel-Rady Ibrahim Mohamed (M'06) was born in Cairo, Egypt, on November 25, 1977. He received the B.Sc. (with Hons.) and M.Sc. degrees in electrical engineering from Ain Shams University, Cairo, in 2000 and 2004, respectively, and the Ph.D. degree in electrical engineering from the University of Waterloo, Waterloo, ON, Canada, in 2008.

He is currently an Assistant Professor in the Department of Electrical and Computer Engineering, University of Alberta, Edmonton, AB, Canada. His research interests include dynamics and controls of power converters, distributed and renewable generation; modeling, analysis, and control of smart grids; and electric machines and motor drives.

Dr. Mohamed is an Associate Editor of the IEEE TRANSACTIONS ON INDUSTRIAL ELECTRONICS. He is also a Guest Editor of the IEEE TRANSACTIONS ON INDUSTRIAL ELECTRONICS Special Section on "Distributed Generation and Micro-grids". His biography is listed in Marque's Who is Who in the World.